iScience

CellPress

Article

Plasmonics Yields Efficient Electron Transport via Assembly of Shell-Insulated Au Nanoparticles

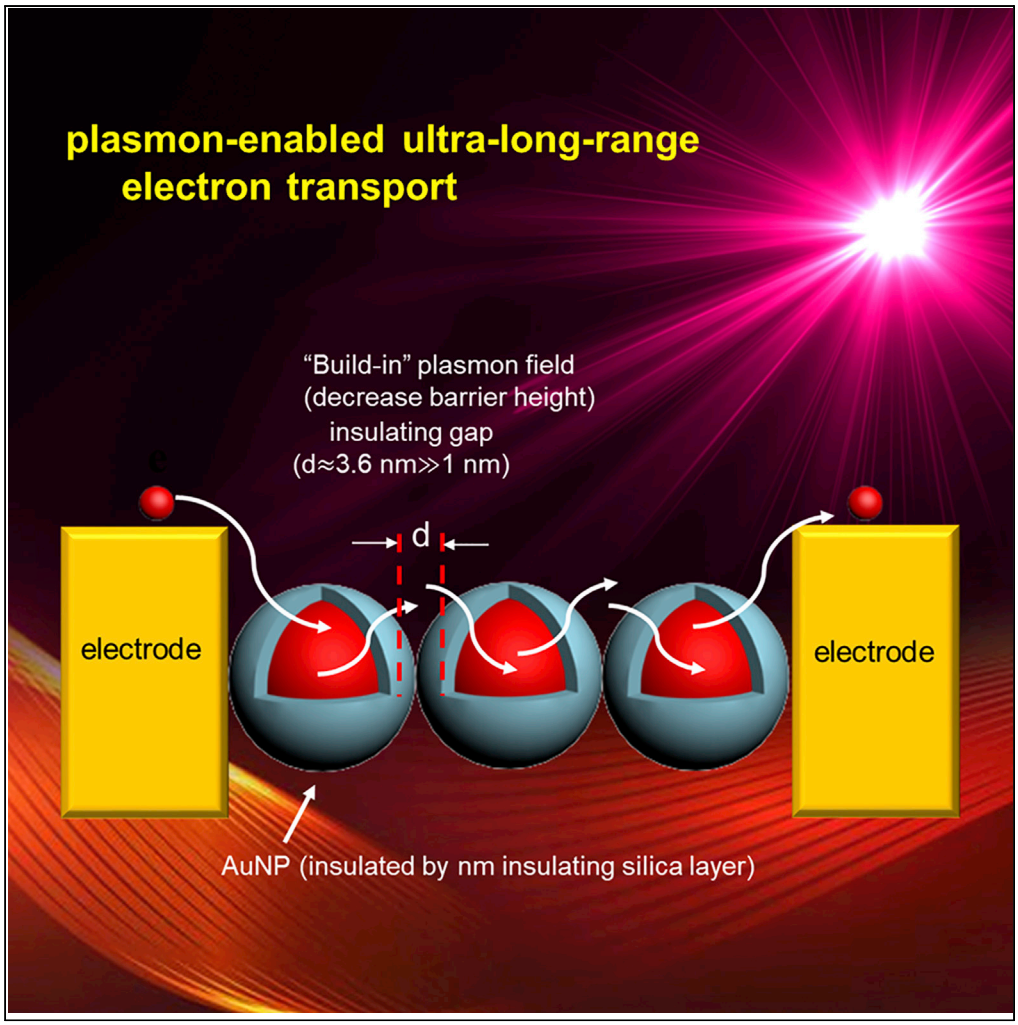

Chuanping Li, David Cahen, Ping Wang, Haijuan Li, Jie Zhang, Yongdong Jin

ydjin@ciac.ac.cn

HIGHLIGHTS

A robust, molecule-free Au@SiO_2 nanofilm-based plasmonic circuit is fabricated

It shows unusual long-range electron transport across AuNPs with 3.6-nm silica gap

LSPR coupling plays a crucial role on the ultra-long-range electron transport

Li et al., iScience 8, 213–221
October 26, 2018
https://doi.org/10.1016/j.isci.2018.09.022

iScience

CellPress

Article

Plasmonics Yields Efficient Electron Transport via Assembly of Shell-Insulated Au Nanoparticles

Chuanping Li,[1,2] David Cahen,[3] Ping Wang,[1] Haijuan Li,[1] Jie Zhang,[1] and Yongdong Jin[1,2,4,*]

SUMMARY

Junctions built from metallic nanoparticles (NPs) can circumvent the diffraction limit and combine molecular/nanoelectronics with plasmonics. However, experimental advances in plasmon-assisted electron transport at the nanoscale have been limited. We construct junctions of a robust, molecule-free, suspended film, built solely from AuNPs, capped by SiO_2 shells (Au@SiO_2), which give insulating tunneling gaps up to 3.6 nm between the NPs. Current measured across monolayers of such AuNPs shows ultra-long-range, plasmon-enabled electron transport (P-transport), beyond the range of normal electron tunneling across insulators. This finding challenges the present understanding of electron transport in such systems and opens possibilities for future combinations of plasmonics and nanoelectronics.

INTRODUCTION

Molecular electronics devices, by using individual molecules as active electronic components (Nitzan and Ratner, 2003) to miniaturize conventional electronic components, hold great promise for electronics applications. However, such tiny devices, with current transport that can be described by accepted electron tunneling theory (Figure 1A), are mostly not robust for reliable practical uses as they often suffer from contact artifacts (Flood et al., 2004; Lau et al., 2004). Therefore, until it matures into a practical technology, alternative solutions to miniaturize devices and/or add functional logic beyond the existing binary ones are desired. Future practical devices may well consist of hybrid devices that combine molecules with nanoelectronics (Cui and Lieber, 2001) and require basic understanding of electron transport at the nanoscale.

Plasmonics, defined as light-metal interactions via coupling with the conduction electrons at the metal-dielectric interface (Fang and Zhu, 2013; Jiang et al., 2014; Ozbay, 2006), converts light into propagating electrical signals and, therefore, merges photonics with electronics at the nanoscale and provides a possible path to next-generation (opto)electronic devices. In the past two decades, the plasmon resonances of metallic nanoparticles (NPs) have been extensively explored for sensitive biosensing and nanomedicine (Anker et al., 2008; Jin et al., 2010), extreme light concentration and manipulation in nanophotonics (Schuller et al., 2010), plasmonic nanochemistry (Baffou and Quidant, 2014), and solar energy harvesting and improved photovoltaic devices (Atwater and Polman, 2010). However, the development of plasmonics for nanoelectronics has been severely hindered by lack of fundamental understanding of plasmon-electron coupling; therefore current studies mainly focus on chemoelectronic circuits (Yan et al., 2016; Schlicke et al., 2015). In principle, plasmons in AuNPs generate an enhanced local electromagnetic field (when compared with Au atoms or bulk Au surfaces) in the "dark" mode; the collective oscillation of the conduction electrons of a AuNP will couple with incident light, upon illumination, to excite the plasmonic "light" mode and enhance further the field. As schematically illustrated in Figures 1B and 1C, when AuNPs, covered with a nanometer-scale insulating gap, are network linked, such inherent "built-in" strong plasmon field and the "dark/light" plasmon modes noted above may have distinct effects on electron transport, lowering barriers and facilitating electron transport across a gap that is larger than what is possible by accepted electron tunneling theory. This might be possible when electron transport meets with "plasmonics," because the extra energy of "hot" electrons (compared with thermally equilibrated ones) makes them more mobile than expected (Najafi et al., 2017). Recently, tunneling plasmons have been probed optically (Savage et al., 2012) and direct observation of, and control over, quantum plasmon resonances at 0.4–1.3 nm length scales across molecular tunnel junctions made of two AgNPs has been achieved (Tan et al., 2014). Very recently, we revealed a long-range plasmon field and plasmoelectronic effect on catalysis (Li et al., 2017). However, *reliable* direct electrical probing of

[1]State Key Laboratory of Electroanalytical Chemistry, Changchun Institute of Applied Chemistry, Chinese Academy of Sciences, 5625 Renmin Street, Changchun 130022, P. R. China

[2]University of Chinese Academy of Sciences, Beijing 100049, P. R. China

[3]Department of Materials and Interfaces, Weizmann Institute of Science, Rehovot 76100, Israel

[4]Lead Contact

*Correspondence: ydjin@ciac.ac.cn

https://doi.org/10.1016/j.isci.2018.09.022

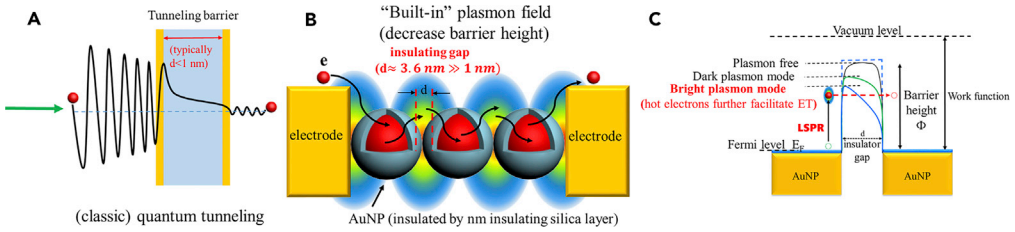

Figure 1. Schematic Illustrations of the Classic Quantum Tunneling and Plasmon-Enabled Long-Range Electron Transport (P-transport) Regime

(A–C) In the P-transport regime (B and C), the inherent "built-in" strong plasmon field (in dark or bright plasmon modes) will facilitate electron transport over lengths beyond that of normal quantum tunneling across an insulating gap (A).

plasmonic effects on long-range electron transport in such nanosystems was not yet achieved and remains a great challenge in this field.

Previously we prepared a simple AuNP monolayer-based planar molecular tunnel junction and observed a plasmon effect, along with AuNP-enhanced current transport through nanometer-scale insulating layers (Jin et al., 2006; Jin and Friedman, 2005). However, such monolayer-based sandwich-type junction devices were not robust enough to rule out possible contact artifacts due to lightning rod effect (Shpaisman et al., 2012) or partially, shorting.

Herein, to eliminate contact artifacts and test the possible plasmonic effects on long-range electron transport, we construct a robust, molecule-free, suspended-film-type plasmonic circuit, based on a mechanically stable enough nanomembrane, made up of a monolayer of pure Au@SiO_2 core-shell NPs (acting as an active component), by bridging it over two micrometer-gap electrodes. This device configuration provides multiple advantages. First, the suspended-film-type junction layout can not only effectively eliminate substrate effects and contact artifacts, rendering the current-carrying device robust to measure and uncover possible plasmonic effects, but also facilitates illumination of the device to study light-induced effects. Second, no additional molecules are introduced into the junction, which can rule out molecule effects and ensures that the observed current and light effects are indeed plasmonic in origin. Third, AuNPs isolated by a nanoscale insulating silica shell can effectively suppress the electronic excitation of plasmons by avoiding direct electric contact between electrodes and AuNPs, which is inevitable if using bare AuNPs in the current-carrying device, making the detection of "real" dark plasmon modes possible. This platform therefore allows us to explore P-transport systematically.

RESULTS

Fabrication and Morphology Analysis of NOE

As depicted in Figures 2A and 2B, the junctions were fabricated by transferring a freshly prepared monolayered nanomembrane gently, via floating from the "soft" air-water interface onto micrometer-gapped Au trench electrodes, as described previously (Wu et al., 2016). The nanomembrane is made of uniform Au@SiO_2 core-shell NPs with Au core diameter of ~12 ± 1.2 nm and homogeneous silica shell thickness of ~1.8 ± 0.5 nm (mean ± TEM, see Figure S1 for detailed characterizations) and was prepared by the method of liquid/liquid interface self-assembly (Shin et al., 2015; Gauvin et al., 2016, please see "Transparent Methods" in the Supplemental Information). Typically, 3 mL colloidal Au@SiO_2 NPs with compact silica shell (prepared and well-characterized according to our previous report (Li et al., 2017, please see "Transparent Methods" in the Supplemental Information) were poured into a plastic container, and 460 μL hexane was added to the solution to form a liquid/liquid interface; then 3.7 mL methanol was poured into the mixture rapidly to capture the NPs at the hexane/water interface. After evaporation of the hexane, the NPs were simultaneously self-assembled into monolayer nanomembranes over a large area at the water/hexane interface and can be seen with the naked eyes (Figure S2A). The freshly prepared nanomembranes were then transferred onto transmission electron microscopic (TEM) grids and Au trench electrodes for TEM and current-voltage (I-V) measurements, respectively. As clearly seen from the gradually zoomed-in TEM images in Figures 2C–2E (Figure S2B shows a higher resolution TEM image of a nanomembrane), the resulting monolayer nanomembranes have AuNPs "jammed" in close contact, but nearly all are well-separated by a transparent gap of ~3.0 ± 0.4 nm (Figure 2F, mean ± TEM). As this gap almost equals twice the silica shell thickness of the NPs, we identify this

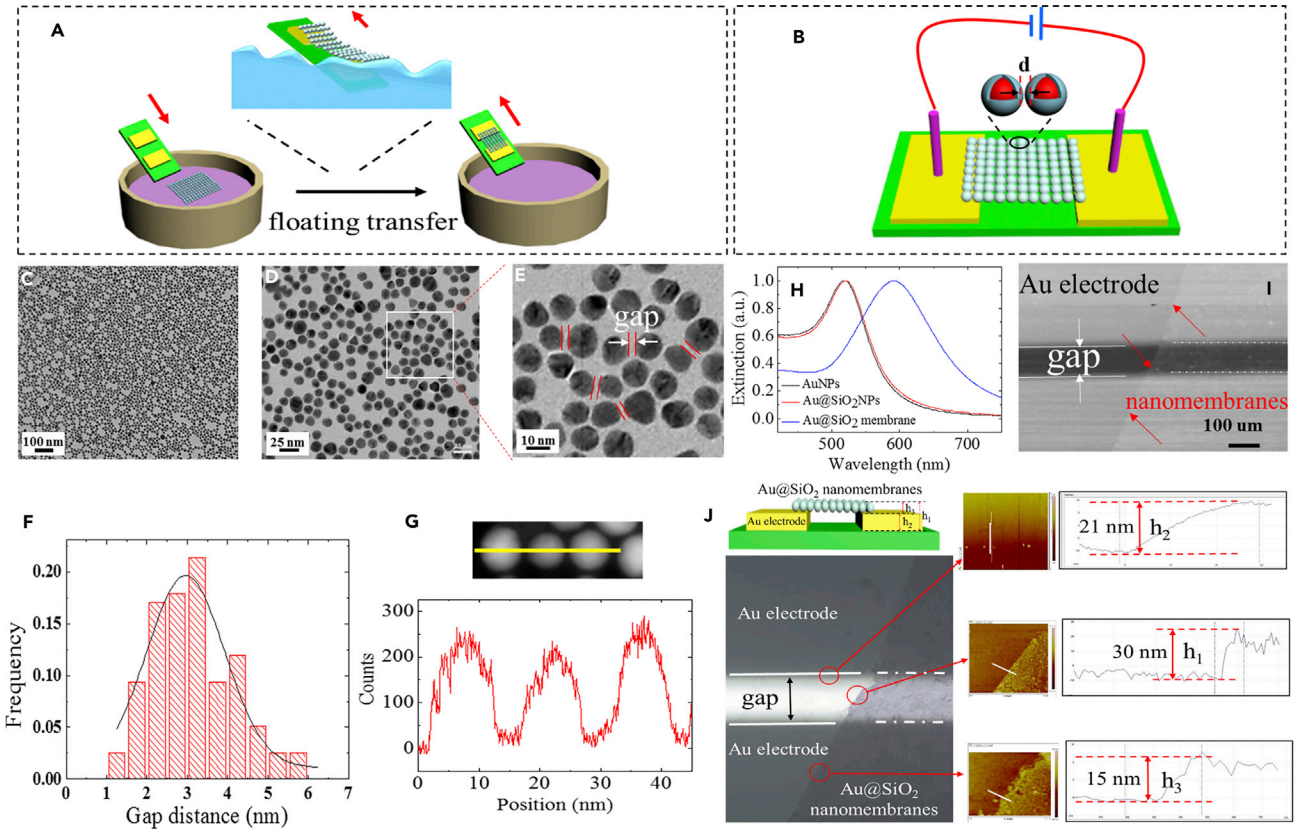

Figure 2. Experimental Device and Nanomembrane Characterizations

(A and B) (A) Schematics of the preparation of the shell-isolated AuNP-based nanomembrane-on-electrode (NOE) via a floating transfer process and (B) the resulting NOE junction configuration.

(C–F) (C–E) Zoomed-in TEM images and (F) gap distance analysis between AuNPs of the monolayered 12 nm Au@1.8 nm SiO_2 nanomembrane, statistically obtained from more than 200 NP pairs. Data are represented as mean ± TEM.

(G) Spherical aberration-corrected scanning TEM image and corresponding (Au) elemental line scan analysis of three adjacent NPs in the 12 nm Au@1.8 nm SiO_2 nanomembrane.

(H) UV-visible spectra of 12 nm AuNPs (black line) and 12 nm Au@1.8 nm SiO_2NPs (red line) in solutions and microscopy-based selected-area bright field extinction spectra of the monolayered 12 nm Au@1.8 nm SiO_2 nanomembrane (blue line).

(I) Typical scanning electron micrograph of the junction.

(J) AFM line scan height profile analysis of the NOE and device. The nanomembrane was maintained intact and suspended bridging over the trench electrodes.

See also Figures S1–S3.

gap as silica. No "fatal" metal (Au) junction or filament formation between adjacent NPs was observed by direct TEM observation (Figure 2E); spherical aberration-corrected scanning TEM elemental line scan analysis (Figure 2G) indicates the stability and shell-isolated nature of the AuNPs. The optical properties of the NPs and the resulting nanomembrane were characterized by UV-visible spectra and microscopy-based selected-area bright field extinction spectra. The plasmon band of the nanomembrane red-shifted from ~519 to 590 nm (Figure 2H) when compared with free AuNPs, which is explained by electromagnetic coupling of the NPs (Jain et al., 2007).

Figure 2I (and Figure S3) shows a typical scanning electron microscopic image of the junction. Impressively, the ultrathin monolayered nanomembrane (~15 nm thick, as measured by atomic force microscopy [AFM]) bridges over the 100-μm gap between the Au trench electrodes, denoted later as nanomembrane-on-electrode (NOE), remaining intact after the floating transfer to prepare the device. The mechanical stiffness and suspended-film geometry of the NOE were further confirmed by AFM line scan height profile analysis of the device (Figure 2J). The robustness of the junction allows making reliable electrical measurements systematically.

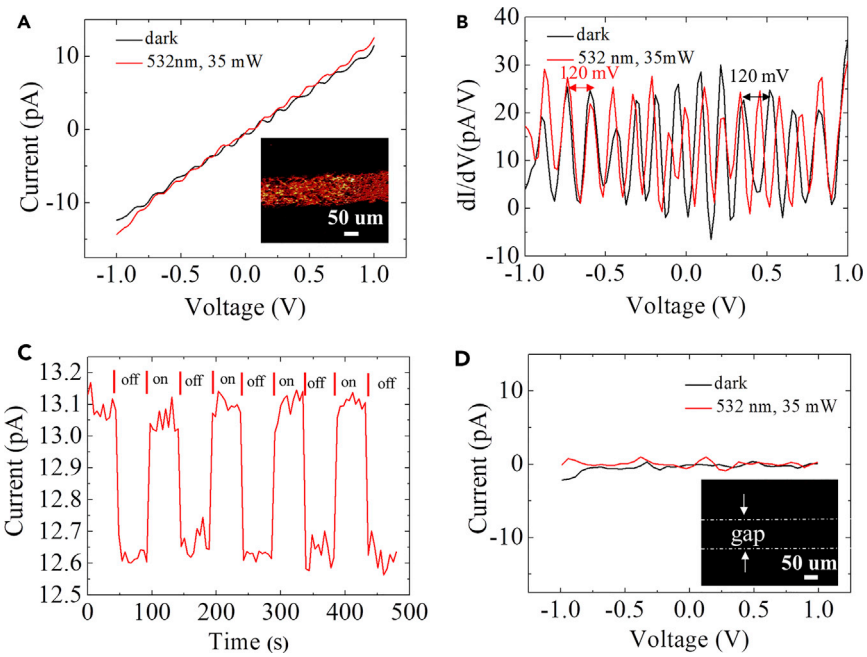

Figure 3. Room Temperature I-V Characteristics of the Junction

(A) Typical room temperature current-voltage (I-V) curve of the junction measured at ambient conditions in a range of ±1 V bias. Inset: microscope-based dark-field scattering image of the NOE nanomembrane.

(B) The corresponding differential conductance curve of the junction obtained numerically from the measured I-V characteristics.

(C) Photoconductance response curves when the light is switched on and off (532 nm, 35 mW).

(D) Typical I-V curve of a control junction fabricated from a plasmonically inactive 12 nm Pd@ 1.6 nm SiO_2 nanomembrane. Inset: microscope-based dark-field scattering image of the NOE nanomembrane.

See also Figures S4–S7, Notes S1 and S2, Scheme S1.

Electrical Characterization of NOE

Figure 3A shows typical room temperature current-voltage (I-V) curve of the junction, measured at ambient conditions over a ±1 V bias range with an NOE-electrode contact edge length of ~2.1 mm (cf. Figure S4 allows contact to ~1.4 × 10^5 Au@SiO_2 NPs at the electrode edge). Remarkably, ~10 pA current flows through the suspended NOE at 1.0 V, which is more than 2 orders of magnitude above our noise level (cf. Figure 3C). If we assume that current flows through all the NPs (i.e., 100% real contact), the junction current at 1 V is calculated to be ~0.1 fA/(NP@contact). Even if this is what remains after passing through a long chain of NPs (~6,500 NPs in series that span the 100-μm gap), this value is still amazing, because the AuNPs in the membrane are well isolated from each other by ~ 3.6-nm insulating silica shells. Electron tunneling through such thick an insulator (with a total cumulative silica shell thickness of ~15 μm) should not be measurable because the probability of electron tunneling (T) is an exponential function of the barrier length, L ($|T(E_F)|^2 \sim e^{-\beta L}$, $\sim 2\times10^{-21}$ for a single 3.6-nm silica gap, where β is the tunneling decay parameter in units of (length)$^{-1}$ and we used value of 13.3/nm for SiO_2) (Müller et al., 2002; Salomon et al., 2003).

Interestingly, the I-V curve (Figure 3A) shows nearly linear Ohmic responses, but with pronounced steps both in the dark and under illumination. Such features are unobservable at room temperature for (silica shell-free) AuNP array-based nanosheets or nanomembranes. Such steps may be caused by both low packing density of the networked nanomembrane (Wu et al., 2016) and the transport barrier, created by the thin silica shells between individual AuNPs. Such curves require k_BT < charging energy; without the silica shell, k_BT > charging energy of the NPs should hold (Liao et al., 2011). Although it is quite difficult to observe the current steps on an irregular thin nanofilm at room temperature, the Coulomb staircase can still be observed in some specific cases, for instance, a granular nanofilm system consists of several thousands of tunnel junctions (Imamura et al., 2000). In our case, the observed Coulomb staircases may be a reflection of (very) limited current transport paths (due to the low packing density) of the NOE NPs and a sign of unusual quantum transport of electrons (P-transport in this study) from grain (AuNP) to grain (AuNPs) through

the intervening amorphous silica shells that act as potential barriers or weak links. The very presence of such current steps in the Au@SiO_2 NPs system suggest that somewhere there is a weak link in what is otherwise a relatively well-conducting system. Also, the observed (overall) Ohmic-like response is quite different from the nonlinear response that typifies the quantum tunneling regime, implying a different electron transport regime. However, the origin for the current steps is still not clear and needs to be further studied.

DISCUSSION

The underlying mechanism was primarily probed by measuring the temperature dependence of its electronic conductivity. From the results presented in Figures S5 and S6A–S6C, the conductance shows weak temperature dependence from room temperature till 200–170 K, below which it is roughly constant, which is consistent with electron tunneling below 170 K. The weak temperature dependence till 170 K, though, is much larger than what is expected from broadening of the Fermi-Dirac distribution of carriers in the electrodes with increasing temperature (Hrach, 1968; Vilan et al., 2017), implying that another mechanism dominates at these higher temperatures. Interestingly, as shown in Figure S7, the step-like current feature remained but became weaker if the I-V measurement was taken at higher temperature (~333 K).

According to a rough estimate based on electron tunneling, using a simplified Wentzel–Kramers–Brillouin (WKB)-based model (Tomfohr and Sankey, 2002), the calculated current across a junction of even one row of Au@SiO_2 NP-bridged NOE (the NOE-electrode contact edge length used in the calculation is the same as that used in the experimental junction, corresponding to Figure S4, i.e., ~2.1 mm) is about 3×10^{-17} A at 1 V (see Note S1), which is far smaller than the detected junction current (~10^{-11} A) for the whole NOE (for an electron to cross the gap between the electrodes ~6,500 sequential tunneling events are needed!).

Considering the tunneling charge transfer plasmon mode reported previously (Tan et al., 2014), we propose that this huge enhancement of electron transport probability and ultra-long-range electron transport ability may be attributed to the plasmonic nature of the Au@SiO_2 nanomembrane and the collective, wave-like charge density fluctuation (localized surface plasmon resonance [LSPR] coupling between adjacent AuNPs and its facilitation for ultra-long-range electron transport) of the 2D plasmonic nanomembranes (Warren et al., 2012).

The plasmonic nature of the NOE was manifested by *in situ* dark-field scattering imaging. As seen from Figure S8, only the NOE bridging over the trench is plasmonically active (survives plasmon damping caused by close electrode contact), and it persists after the successive I-V measurements. As current cannot flow through the blank Au-Au microtrench electrodes (Figure S9), and control devices using NOE made of bare AuNPs (without silica shell) displayed only Ohmic I-V response with current range in microamperes (Figure S10A) due to metallic Ohmic contact between adjacent AuNPs and hence partial plasmon damping of the NOE as revealed by TEM (Figure S10B) and dark-field image (Figure S10C), the observed I-V characteristics are therefore attributed to the physical properties of the NPs and NOE.

Figure 3B shows the differential conductance curve of the junction obtained by numerical differentiation of the measured I-V characteristics. The peaks are clearly seen with an average step width of about 120 mV, but they are not very periodic, possibly due to the complex 2D nanostructure and uncontrollable multiple electron tunneling paths of the NOE junction system. The value (120 mV) was then used to estimate the capacitance of the Au@SiO_2 NPs ($C \approx e/\Delta V = 1.3\times10^{-18}$ F), which matches the calculated value (~4×10^{-18} F) (see Note S2). Because in the present junction system

(1) the charging energy of the NPs (~1.4×10^{-19} J) is much larger than the thermal energy k_BT (4×10^{-21} J) and

(2) the resistance of the junction (~$10^{11}\Omega$ for NOE) is larger than the quantum resistance ($\hbar/e^2 = 2.6\times10^4$ Ω) (Note S2),

we suggest that the ultra-long-distance electron transport through the NOE is due to the unique capacitive and plasmonic properties of the NPs. Then, the observed Coulomb staircases might be a reflection of Coulomb charging at room temperature. Measurements on the same devices through successive potential cycling showed very reproducible I-V characteristics and indicated reliable stable contact formation. Thanks to the solid contact of NPs (via assembly) and robustness of the NOE junctions (cf. Figure 2J),

the I-V responses were quite reproducible from device to device with the same preparation (in the same order of magnitude, ~ dozens of picoamperes, see Figure S11), further ruling out contact artifacts. Control experiments of the NOE junction made of big AuNPs (~32 nm) with similar 1.6-nm silica shells showed similar I-V response but strongly weakened Coulomb staircases due to the size increase and the loss of NP homogeneity (Figure S12). We also examined the effect of the SiO_2 shell thickness on the electron transport behavior of the assemblies. With an ultrathin silica shell coating of ~1.1 ± 0.6 nm (Figure S13A), the I-V curves changed from linear, i.e., Ohmic (for the non-coated AuNPs, cf. Figure S10A) to non-linear, accompanied by a pronounced current drop from micro- to nanoamperes (at −1 V applied bias) and some step-like features (Figure S13B). With even a slight increase of silica shell thickness to the typical 1.8 ± 0.5 nm (Figure S1A, mean ± TEM), pronounced steps appear in the current curves (cf. Figure 3A). However, increasing the silica shell thickness further to ~3.0 nm, no current was measured through the NOE junctions (Figure S14), as the ~6-nm SiO_x barrier likely decreases tunneling probability below our measurement limits (with nearly the same NOE-electrode contact edge length of about 2.5 mm).

Although efficient (measurable) electron tunneling through ~3.6-nm insulating silica gap seems not possible, clearly electron transport occurs, not across one, but across >6,000 such junctions; this may be enabled by the strong "built-in" long-range plasmon field and mediated by "dark/light" plasmon modes of the NP system (cf. Figures 1A–1C). As shown in Figure 3A, in the dark the junction carries a current of approximately −12.3 pA at −1 V applied bias, uncovering for the first time (to the best of our knowledge) the "dark" plasmon mode and its contribution to current transport, which is hard to be revealed in a current-carrying device if using bare AuNPs since electronically excited plasmons (or hot electrons) will overlay onto it. Upon irradiation with light (35 mW), the conductance increases slightly to −13.5 pS (the relatively low laser intensity efficiently limits any possible direct photothermal heating effect on the electron transport), due to the excitation of additional plasmons optically. Upon turning off the light, the conductance decreased immediately to the original "dark" value. This can be cycled between these two states by alternating turn on/off light (Figure 3C). As closely seen from Figure 3C, under successive ~1 min illumination the photoconductance fluctuation was maintained within the noise level (~0.1 pS, cf. ~ 1.2 pS for photoresponse in Figure 3A), i.e., no detectable drift in photoconductance occurred, which in fact can rule out the photothermal effect. More importantly, when we used both non-plasmonic metallic Pd NPs (~12 nm) with similar 1.6-nm silica shells and insulating SiO_2 NPs (with even larger NOE-electrode contact edge length of ~2.9 mm, Figures S15B and S16D) to prepare NOE junctions, no electron transport was detected for these junctions as shown in Figures 3D and S15 (see Figure S16 for detailed characterizations). This is consistent with the plasmonic origin of the observed effects.

The plasmonic nature and "light" mode effect of the electron transport phenomenon was further confirmed by illumination-wavelength- and intensity-dependent I-V measurements of the NOE junctions. As shown in Figure 4A, illuminating the NOE with green (λ = 532 nm), blue (λ = 450 nm), and red (λ = 650 nm) lights with comparable light intensity (35 mW) causes an obvious increase in the junction conductance over that of the dark conductance, and the conductance with green light (more spectral overlap with monolayered nanomembrane's plasmon resonance spectrum) is obviously larger than that with other lights, which fits quite well with the LSPR band profile of the NPs (Figure 4B). The junction conductance also increases with the increase of illumination intensity (Figure 4C). This is consistent with the contribution of the photo-induced "hot electron," whose effect on photocurrent is dependent on the irradiation intensity (Conklin et al., 2013). Since the temperature increase on NP surfaces is roughly estimated to be well below 1°C in our system (Qin and Bischof, 2012, Note S3), it cannot be the main driving force for the observed electron transport enhancement. In fact, the locally generated small amount of heat within the suspended ultrathin NOE nanomembrane can be further dissipated either laterally (via electron flow) or vertically (via ambient air). This has been further proved by photothermal imaging of the real temperature variation of the NOE junction during the light on/off I-V measurements (Figure S17). The observed electron transport (ET) enhancement is, therefore, primarily a (non-photothermal) plasmon effect.

Figure 4D shows the result of finite difference time domain simulation (FDTD), displaying a remarkably enhanced electromagnetic field between adjacent NPs. Although the frequencies associated with the electron flow are much lower than the frequency variation of the enhanced electric field due to irradiation (~10^{14} Hz), they merge at the nanoscale with "plasmonics," and the plasmon-induced strong localized "built-in" electromagnetic near fields, along with collective wavelike charge density fluctuation at the nanoscale (Ambrosetti et al., 2016), are possibly supposed to facilitate electron tunneling between proximal

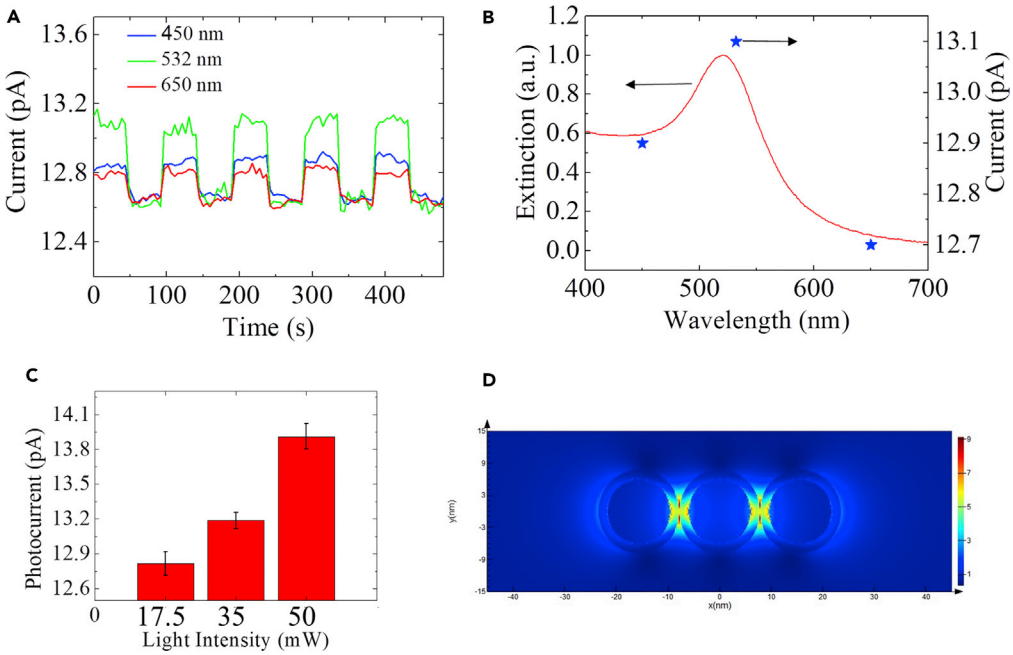

Figure 4. Illumination Wavelength- and Intensity-Dependent Junction Conductance of the NOE Junctions

(A and B) (A) Illumination wavelength-dependent photoconductance of the NOE junctions, which fits well with (B) the extinction profile of the AuNPs.

(C) Illumination intensity-dependent photoconductance of the NOE junctions. Data are represented as mean ± photoconductance.

(D) FDTD simulation of the electric field distribution of three closely impacted 12 nm Au@1.8 nm SiO_2 NPs.

See also Figures S8–S18, Note S3.

AuNPs and current flow across the NOE. However, further investigations are needed to finally reveal the whole story of P-transport, including how it scales.

Conclusion

By constructing a robust suspended-film-type plasmoelectronic circuit, using shell-isolated Au@SiO_2 NPs as building blocks, we have revealed a new electron transport regime—plasmon-enabled/plasmon-coupled long-range electron transport (P-transport) on the 2D metasurface. Unprecedented long-range electron transport across the monolayered jammed AuNPs with insulating tunneling gap up to 3.6 nm, which is impossible for the currently accepted electron tunneling theory, are observed. The crucial role of the LSPR coupling (collective wave-like charge density fluctuation and surfing of electrons) in P-transport was evidenced by photocurrent enhancement, wavelength-dependent current intensity, and FDTD simulation of the electric field distribution. The finding reshapes our thinking on fundamental electron transport regimes on the nanoscale, will open an interdisciplinary field of exploration, and will promote future development of plasmoelectronics, integrating plasmonics with nanoelectronics.

Limitations of Study

The origin for the current steps is not clear and needs to be further studied; issues with reproducibility and control of the structures also warrant further studies.

METHODS

All methods can be found in the accompanying Transparent Methods supplemental file.

SUPPLEMENTAL INFORMATION

Supplemental Information includes Transparent Methods, 18 figures, 1 scheme, and 3 notes and can be found with this article online at https://doi.org/10.1016/j.isci.2018.09.022.

ACKNOWLEDGMENTS

C.L. thanks Y. Tian (from Jilin University) for the FDTD simulation of the electric field distribution and Z.Q. Wang and X.H. Li (all from Northeast Normal University) for facilitating the temperature-dependent I-V measurement. Y.J. acknowledges support from the National Key Research and Development Program of China (Grant No. 2016YFA0201300), the Natural Science Foundation of China (Grant Nos.21475125 and 21675146) and the Instrument Developing Project of the Chinese Academy of Sciences (Grant No. YZ201666).

AUTHOR CONTRIBUTIONS

Y.J. conceived and designed the project. C.L. prepared the nanomaterials and devices, conducted the structural and optical characterizations, and performed electrical measurements. C.L., P.W., H.L., J.Z., D.C., and Y.J. analyzed and discussed the data. Y.J., C.L. and D.C. wrote the paper.

DECLARATION OF INTERESTS

The authors declare no competing interests.

Received: June 6, 2018
Revised: August 27, 2018
Accepted: September 25, 2018
Published: October 26, 2018

REFERENCES

Ambrosetti, A., Ferri, N., DiStasio, R.A., and Tkatchenko, A. (2016). Wavelike charge density fluctuations and van der Waals interactions at the nanoscale. Science *351*, 1171–1176.

Anker, J.N., Hall, W.P., Lyandres, O., Shah, N.C., Zhao, J., and Van Duyne, R.P. (2008). Biosensing with plasmonic nanosensors. Nat. Mater. *7*, 442–453.

Atwater, H.A., and Polman, A. (2010). Plasmonics for improved photovoltaic devices. Nat. Mater. *9*, 205–213.

Baffou, G., and Quidant, R. (2014). Nanoplasmonics for chemistry. Chem. Soc. Rev. *43*, 3898–3907.

Conklin, D., Nanayakkara, S., Park, T.-H., Lagadec, M.F., Stecher, J.T., Chen, X., Therien, M.J., and Bonnell, D.A. (2013). Exploiting plasmon-induced hot electrons in molecular electronic devices. ACS Nano *7*, 4479–4486.

Cui, Y., and Lieber, C.M. (2001). Functional nanoscale electronic devices assembled using silicon nanowire building blocks. Science *291*, 851–853.

Fang, Z., and Zhu, X. (2013). Plasmonics in nanostructures. Adv. Mater. *25*, 3840–3856.

Flood, A.H., Stoddart, J.F., Steuerman, D.W., and Heath, J.R. (2004). Whence molecular electronics? Science *306*, 2055–2056.

Gauvin, M., Alnasser, T., Terver, E., Abid, I., Mlayah, A., Xie, S., Brugger, J., Viallet, B., Ressier, L., and Grisolia, J. (2016). Plasmonic photo-current in freestanding monolayered gold nanoparticle membranes. Nanoscale *8*, 16162–16167.

Hrach, R. (1968). A contribution to the temperature dependence of the tunnel current of metal-dielectric-metal structures. Czech. J. Phys. B *18*, 402–418.

Imamura, H., Chiba, J., Mitani, S., Takanashi, K., Takahashi, S., Maekawa, S., and Fujimori, H. (2000). Coulomb staircase in STM current through granular films. Phys. Rev. B *61*, 46–49.

Jain, P.K., Huang, W., and El-Sayed, M.A. (2007). On the universal scaling behavior of the distance decay of plasmon coupling in metal nanoparticle pairs: a plasmon ruler equation. Nano Lett. *7*, 2080–2088.

Jiang, R., Li, B., Fang, C., and Wang, J. (2014). Metal/semiconductor hybrid nanostructures for plasmon-enhanced applications. Adv. Mater. *26*, 5274–5309.

Jin, Y., Cahen, D., Friedman, N., and Sheves, M. (2006). Gold-nanoparticle-enhanced current transport through nanometer-scale insulating layers. Angew. Chem. Int. Ed. *118*, 6473–6476.

Jin, Y., and Friedman, N. (2005). Surface plasmon resonance-mediated colloid gold monolayer junctions. J. Am. Chem. Soc. *127*, 11902–11903.

Jin, Y., Jia, C., Huang, S.-W., O'Donnell, M., and Gao, X. (2010). Multifunctional nanoparticles as coupled contrast agents. Nat. Commun. *1*, 41.

Lau, C.N., Stewart, D.R., Williams, R.S., and Bockrath, M. (2004). Direct observation of nanoscale switching centers in metal/molecule/metal structures. Nano Lett. *4*, 569–572.

Li, C., Wang, P., Tian, Y., Xu, X., Hou, H., Wang, M., Qi, G., and Jin, Y. (2017). Long-range plasmon field and plasmoelectric effect on catalysis revealed by shell-thickness-tunable pinhole-free Au@SiO2 core–shell nanoparticles: a case study of p-nitrophenol reduction. ACS Catal. *7*, 5391–5398.

Liao, J., Zhou, Y., Huang, C., Wang, Y., and Peng, L. (2011). Fabrication, transfer, and transport properties of monolayered freestanding nanoparticle sheets. Small *7*, 583–587.

Müller, K.-H., Herrmann, J., Raguse, B., Baxter, G., and Red, T. (2002). Percolation model for electron conduction in films of metal nanoparticles linked by organic molecules. Phys. Rev. B *66*, 075417.

Najafi, E., Ivanov, V., Zewail, A., and Bernardi, M. (2017). Super-diffusion of excited carriers in semiconductors. Nat. Commun. *8*, 15177.

Nitzan, A., and Ratner, M.A. (2003). Electron transport in molecular wire junctions. Science *300*, 1384–1389.

Ozbay, E. (2006). Plasmonics: merging photonics and electronics at nanoscale dimensions. Science *311*, 189–193.

Qin, Z.P., and Bischof, J.C. (2012). Thermophysical and biological responses of gold nanoparticle laser heating. Chem. Soc. Rev. *41*, 1191–1217.

Salomon, A., Cahen, D., Lindsay, S., Tomfohr, J., Engelkes, V.B., and Frisbie, C.D. (2003). Comparison of electronic transport measurements on organic molecules. Adv. Mater. *15*, 1881–1890.

Savage, K.J., Hawkeye, M.M., Esteban, R., Borisov, A.G., Aizpurua, J., and Baumberg, J.J. (2012). Revealing the quantum regime in tunnelling plasmonics. Nature *491*, 574–577.

Schlicke, H., Battista, D., Kunze, S., Schröter, C.J., Eich, M., and Vossmeyer, T. (2015). Freestanding membranes of cross-linked gold nanoparticles:

novel functional materials for electrostatic actuators. ACS Appl. Mater. Interfaces *7*, 15123–15128.

Schuller, J.A., Barnard, E.S., Cai, W., Jun, Y.C., White, J.S., and Brongersma, M.L. (2010). Plasmonics for extreme light concentration and manipulation. Nat. Mater. *9*, 193–204.

Shin, Y., Song, J., Kim, D., and Kang, T. (2015). Facile preparation of ultrasmall void metallic nanogap from self-assembled gold–silica core–shell nanoparticles monolayer via kinetic control. Adv. Mater. *27*, 4344–4350.

Shpaisman, H., Cohen, H., Har-Lavan, R., Azulai, D., Stein, N., and Cahen, D. (2012). A novel method for investigating electrical breakdown enhancement by nm-sized features. Nanoscale *4*, 3128–3134.

Tan, S.F., Wu, L., Yang, J.K., Bai, P., Bosman, M., and Nijhuis, C.A. (2014). Quantum plasmon resonances controlled by molecular tunnel junctions. Science *343*, 1496–1499.

Tomfohr, J.K., and Sankey, O.F. (2002). Simple estimates of the electron transport properties of molecules. Phys. Status Solidi B *233*, 59–69.

Vilan, A., Aswal, D., and Cahen, D. (2017). Large-area, ensemble molecular electronics: motivation and challenges. Chem. Rev. *117*, 4248–4286.

Warren, S.C., Walker, D.A., and Grzybowski, B.A. (2012). Plasmoelectronics: coupling plasmonic excitation with electron flow. Langmuir *28*, 9093–9102.

Wu, H., Li, C., Zhao, Z., Li, H., and Jin, Y. (2016). Free-Standing monolayered metallic nanoparticle networks as building blocks for plasmonic nanoelectronic junctions. ACS Appl. Mater. Interfaces *8*, 1594–1599.

Yan, Y., Warren, S.C., Fuller, P., and Grzybowski, B.A. (2016). Chemoelectronic circuits based on metal nanoparticles. Nat. Nanotechnol. *11*, 603–608.

ISCI, Volume *8*

Supplemental Information

Plasmonics Yields Efficient Electron Transport via Assembly of Shell-Insulated Au Nanoparticles

Chuanping Li, David Cahen, Ping Wang, Haijuan Li, Jie Zhang, and Yongdong Jin

Supplemental Information

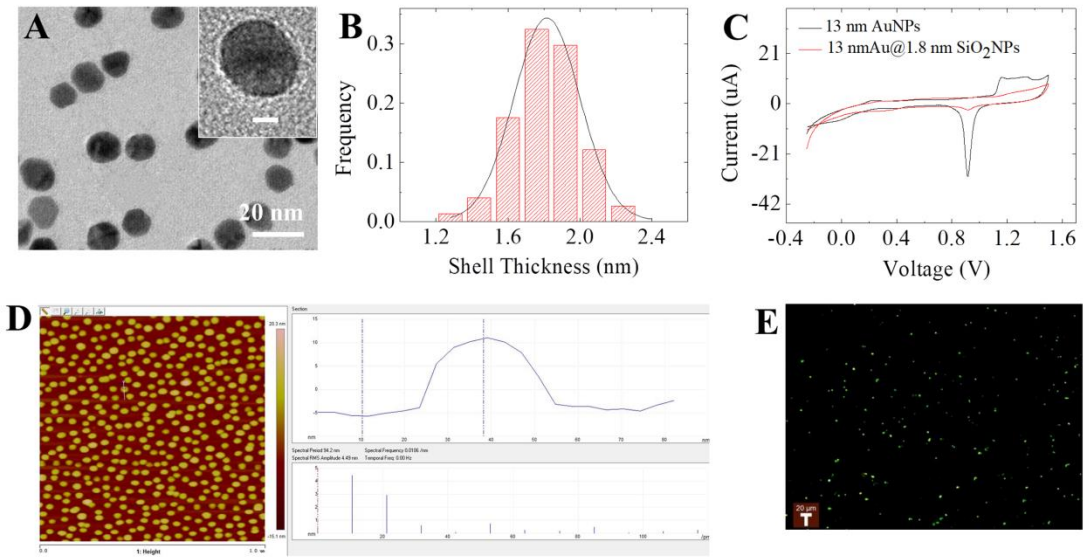

Figure S1. Characterization of 12 nm Au@1.8 nm SiO_2 NPs. (A-B) Typical TEM image and silica shell thickness analysis of the 12 nm Au@1.8 nm SiO_2 NPs. Inset scale bar: 5 nm. Data are represented as mean ± TEM. (C) Cyclic voltammetry curves of 12 nm AuNPs and 12 nm Au@1.8 nm SiO_2 NPs measured in 0.1 M diluted H_2SO_4 aqueous solution at 20 mV/s; (D) AFM line scan height profile analysis and (E) dark-field image of the 12 nm Au@1.8 nm SiO_2 NPs. Related to Figure 2.

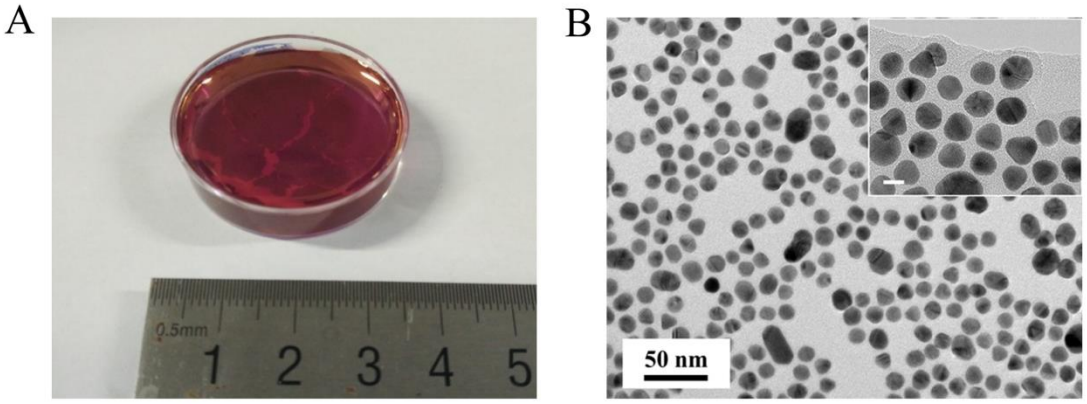

Figure S2. Characterization of Au@SiO_2 nanomembranes. (A) Optical image and (B) TEM images of the as-prepared 12 nm Au@1.8 nm SiO_2 monolayered nanomembranes. Inset bar: 10 nm. Related to Figure 2.

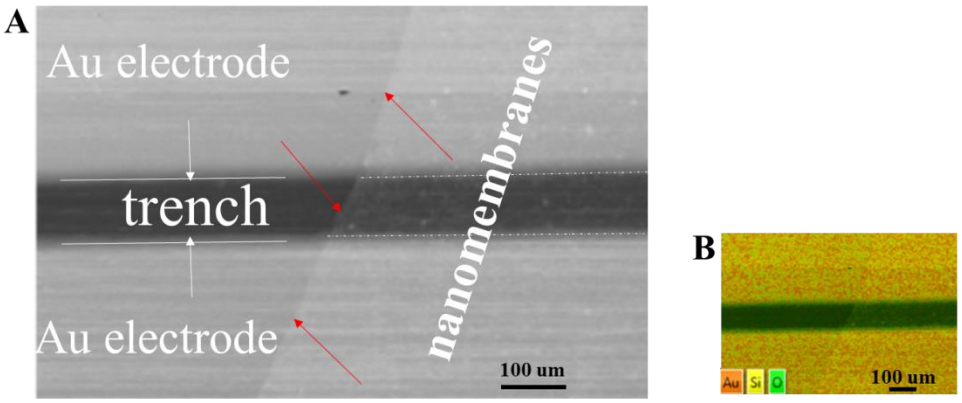

Figure S3. SEM images of the junction. Large scale feature of SEM image and corresponding elemental mapping of the junction made of Au@SiO_2 monolayered nanomembrane, bridging over the 100 μm-gap Au trench electrodes. Related to Figure 2.

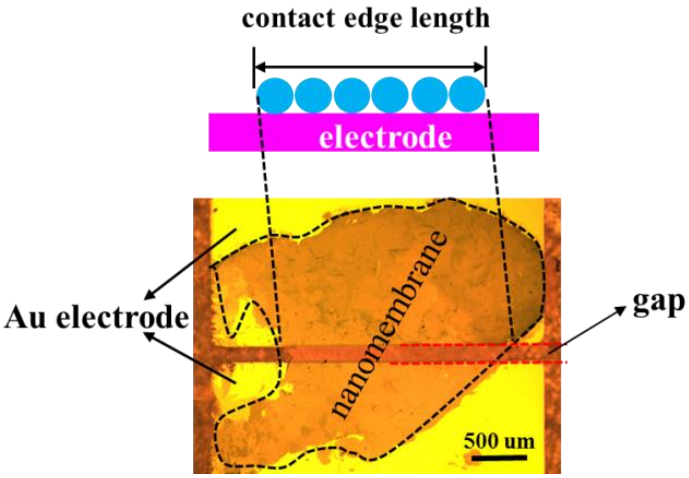

Figure S4. Optical image and the contact edge length of the NOE corresponding to Figure 3. Assuming that it is mostly the leading edge of the membrane on the Au electrode that matters, as the rest will be more resistive, the corresponding leading contact edge lengths are about 2.1 mm. Related to Figure 3.

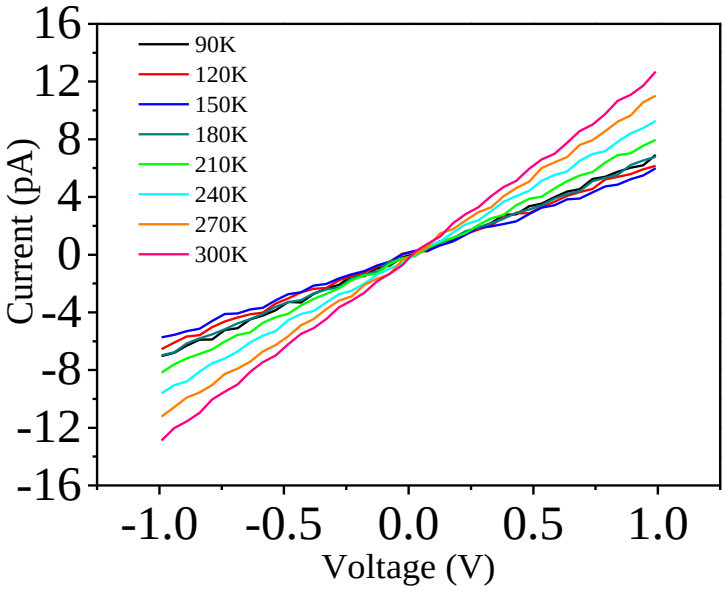

Figure S5. I-V curves of Au/nanoAuNP@SiO_2 membrane/Au (NOE) junction measured for temperatures between 90K-300K. Related to Figure 3.

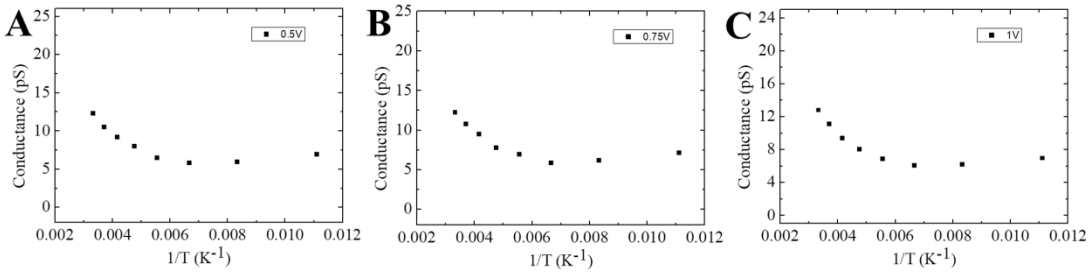

Figure S6. Curves of the temperature dependence of the electronic conductivity of NOE. The data are not well described by the main electronic transport models, but it is possible that at higher temperatures (left) thermally activated transport (possibly hopping between NPs) occurs and at lower temperatures tunneling dominates, even though the suggestive slight increase with further temperature decrease warrants further study. Related to Figure 3.

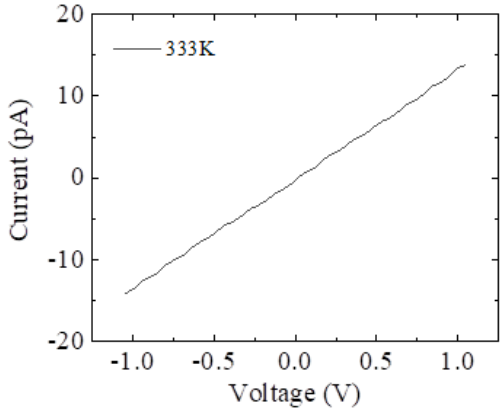

Figure S7. I-V curves of the NOE measured at 333K. Related to Figure 3.

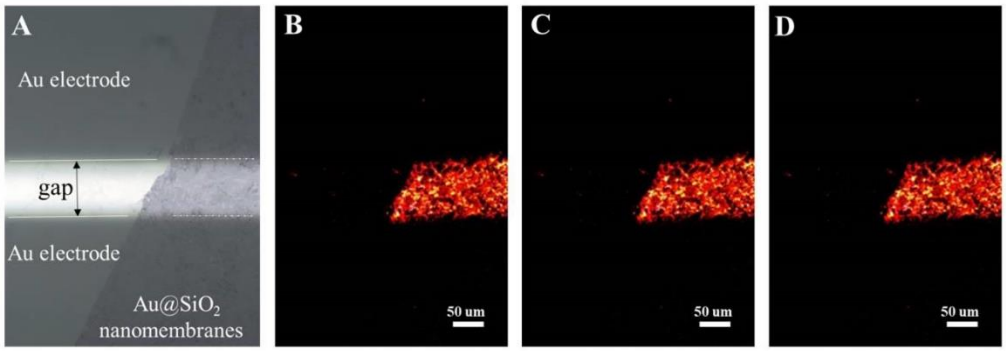

Figure S8. In-situ plasmonic dark-field images of the junction. (A) Optical image of the junction fabricated from 12 nm Au@1.8 nm SiO_2 nanomembrane, and its corresponding in-situ plasmonic dark-field images before (B), during (C) and after (D) the successive I-V measurements. Related to Figure 4.

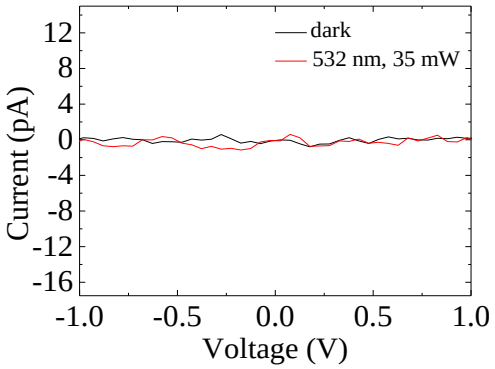

Figure S9. Typical (noise-level) I-V response of the blank (without nanomembrane) Au-Au micro-trench electrodes. Related to Figure 4.

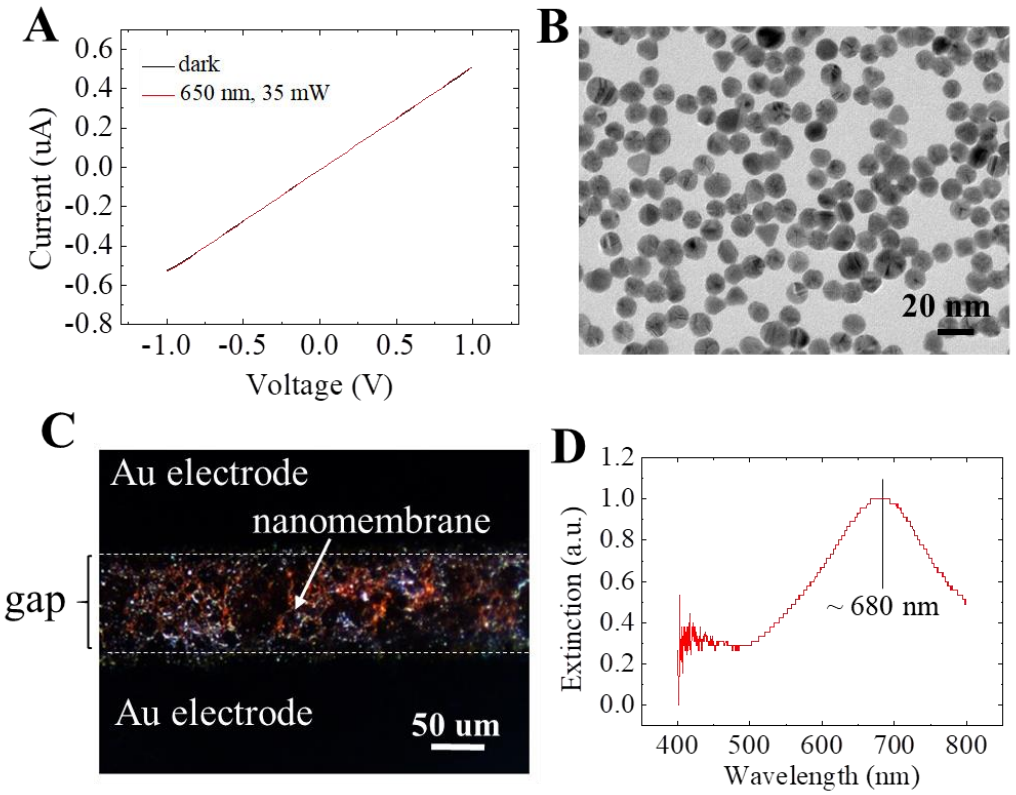

Figure S10. Characterization of 12 nm AuNPs based junction. (A) Typical I-V curves of the junction fabricated from 12 nm AuNPs (without silica shells). TEM image (B), dark-field image (C) and corresponding microscopy-based selected-area dark field scattering spectra of 12 nm Au monolayered nanomembrane (D). Related to Figure 4.

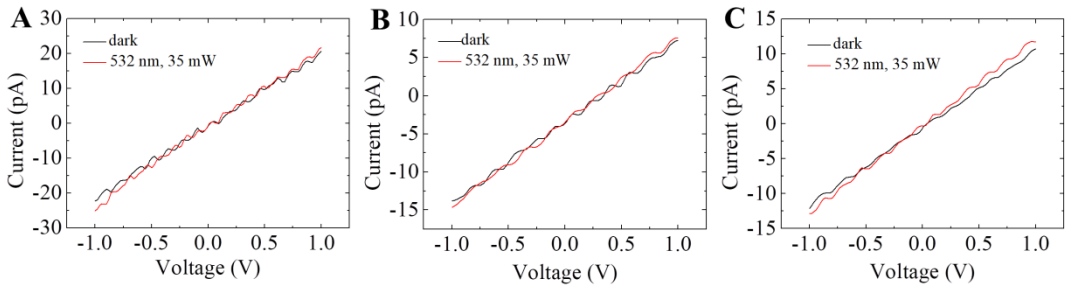

Figure S11. Room-temperature I−V curves of three different devices made of 12 nm Au@1.8 nm SiO_2 nanomembrane, measured at ambient conditions over a ± 1 V in the dark and under 532 nm laser illumination (35 mW) (the corresponding contact edge lengths are ~ 2.7 mm, 1.3 mm, 1.9 mm, respectively). Related to Figure 4.

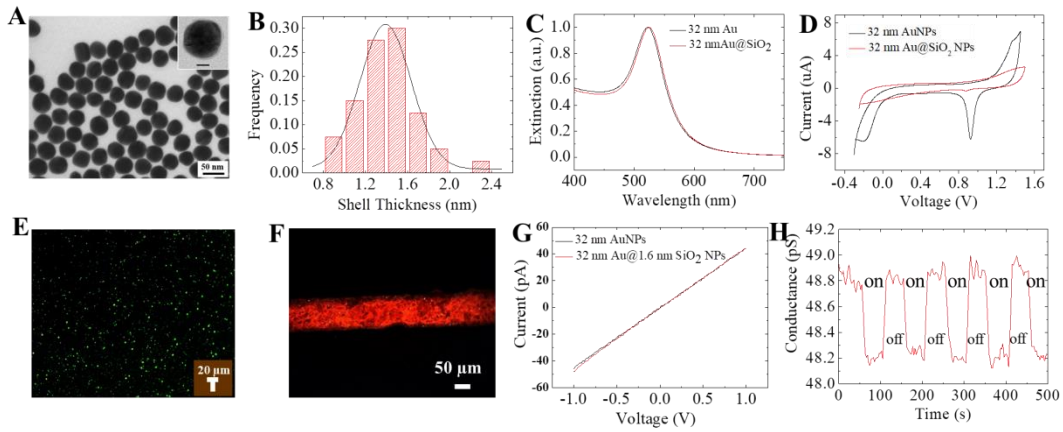

Figure S12. Characterization of 32 nm Au@1.6 nm SiO_2 and corresponding junction. (A) TEM image of the 32 nm Au@1.6 nm SiO_2 NPs. Scale bar of the inset image: 10 nm. (B) Silica shell thickness statistical analysis of 32 nm Au@1.6 nm SiO_2 NPs. Data are represented as mean ± TEM. (C) UV-Vis spectra of 32 nm AuNPs and 32 nm Au@ 1.6 nm SiO_2 NPs. (D) CV curves of 32 nm AuNPs and 32 nm Au@ 1.6 nm SiO_2 NPs measured in 0.1 M diluted H_2SO_4 aqueous solution at 20 mV/s. (E) Dark field scattering image of the 32 nm Au@1.6 nm SiO_2 NPs, dispersed in water. (F) Typical dark-field scattering image of the 32 nm Au@1.6 nm SiO_2 monolayered nanomembranes. (G) Room-temperature I−V curves of the 32 nm Au@1.6 nm SiO_2 nanomembrane, measured in ambient conditions over a ± 1 V range in the dark and under 532 nm laser illumination (35 mW). (H) Photo-conductance responses and stability of the nano-junctions when the light is switched on and off. Related to Figure 4.

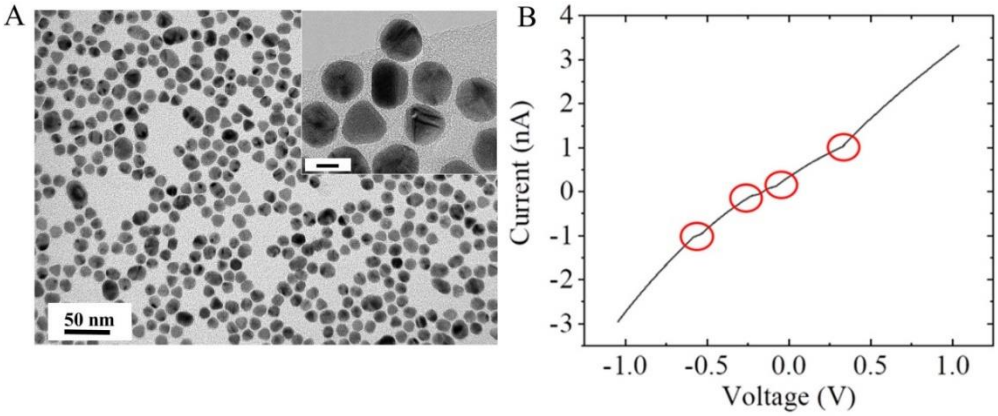

Figure S13. Characterization of 12±1. 2 nm Au@1.1±0. 6 nm SiO_2 NPs and corresponding junction. (A) TEM image of the 12±1.2 nm Au@1.1±0.6 nm SiO_2 NPs. Inset bar: 5 nm. (B) Typical I-V curve of the NOE fabricated by using the 12 nm Au@1.1 nm SiO_2 NPs. The red cycle is the step-like wiggles. Related to Figure 4.

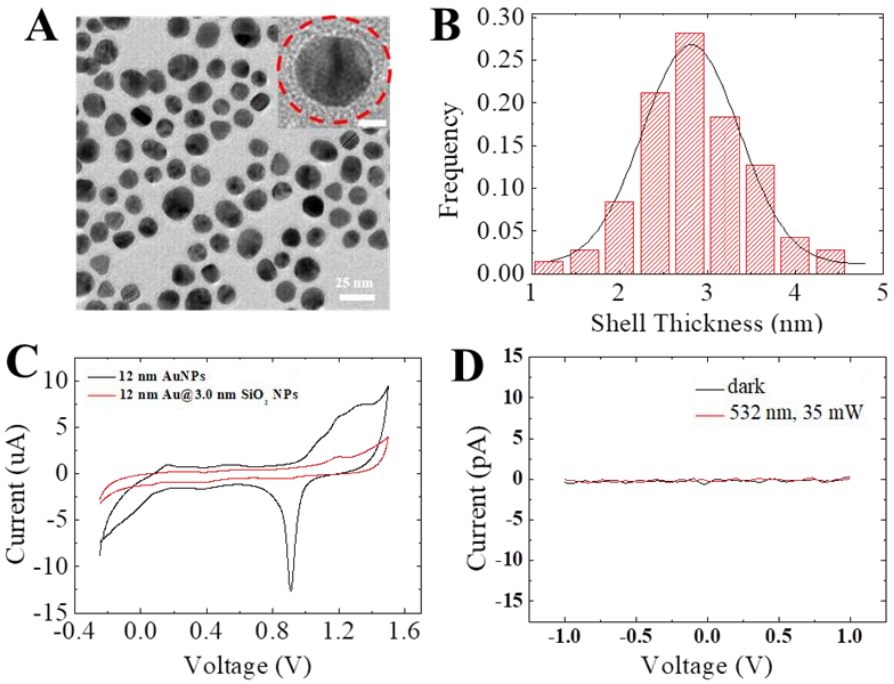

Figure S14. Characterization of 12nm Au@3.0 nm SiO_2 NPs and corresponding I-V behavior of the junction. (A) TEM image of the 12 nm Au@3.0 nm SiO_2 NPs. (B) Silica shell distribution of the 12 nm Au@3.0 nm SiO_2 NPs. Data are represented as mean ± TEM. (C) CV curves of 12 nm AuNPs and 12 nm Au@3.0 nm SiO_2NPs measured in 0.1 M diluted H_2SO_4 aqueous solution at 20 mV/s. (D) Room-temperature I−V curves of the 12 nm Au@3.0 nm SiO_2 nanomembrane measured at ambient conditions over a ± 1 V range, in the dark and under 532 nm laser illumination (35 mW). Related to Figure 4.

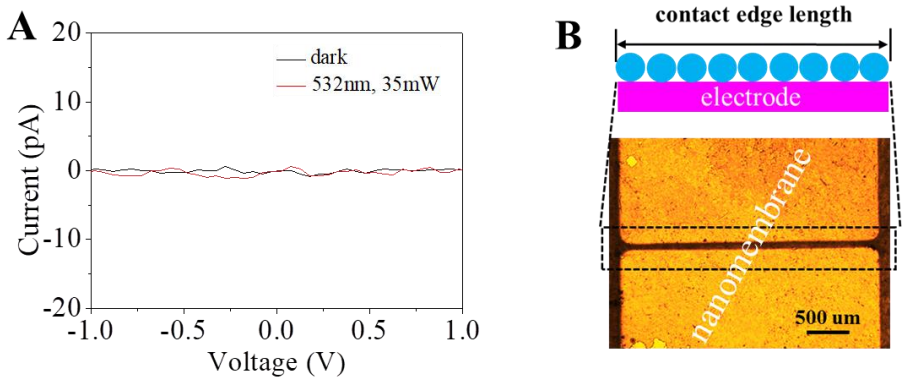

Figure S15. I-V curves of SiO_2 nanomembrane based junction. Typical I-V curve (A) and microscope image (B) of a control junction fabricated from SiO_2 nanomembrane. Related to Figure 4.

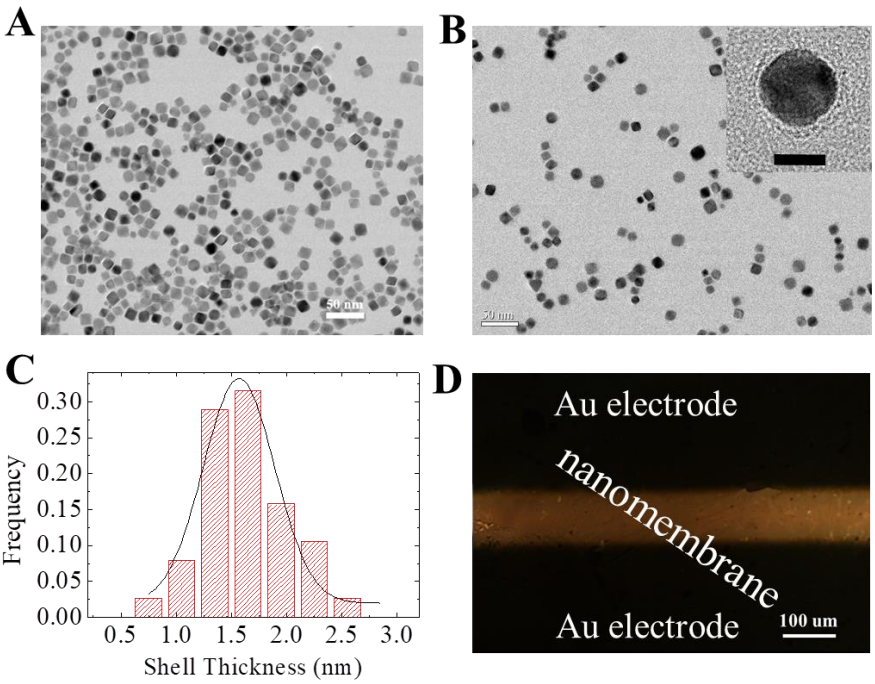

Figure S16. Characterization of 12 nm Pd@1.6 nm SiO_2NPs. TEM images of the non-plasmonic 12 nm Pd NPs (A) and 12 nm Pd@1.6 nm SiO_2 NPs (B). Inset scale bar: 10 nm. (C) Silica shell thickness distribution of the 12 nm Pd@1.6 nm SiO_2 NPs. Data are represented as mean ± TEM. (D) Optical image of a NOE junction fabricated from 12 nm Pd@1.6 nm SiO_2 NPs (length of contact edge here is ~ 2.9 mm). Related to Figure 4.

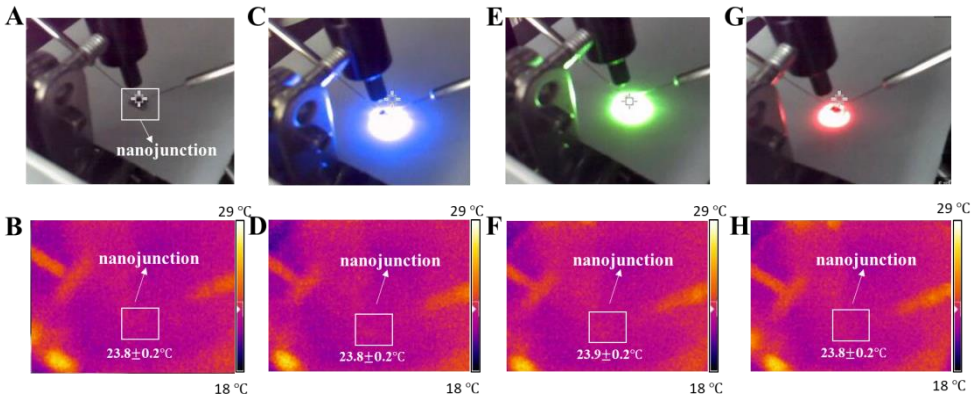

Figure S17. Optical and photothermal imaging of the NOE junction during the I-V measurements. (A, B) in the dark and under illumination with lasers of different wavelengths: 450 nm (C, D), 532 nm (E, F), 650 nm (G, H). In all cases the illumination intensity is 35 mW. Note: The method of photothermal imaging is sensitive enough since obvious infrared thermal image difference of an NOE device can be observed even though the temperature difference is only ~ 2.8 ℃ (see Figure S 18). Related to Figure 4.

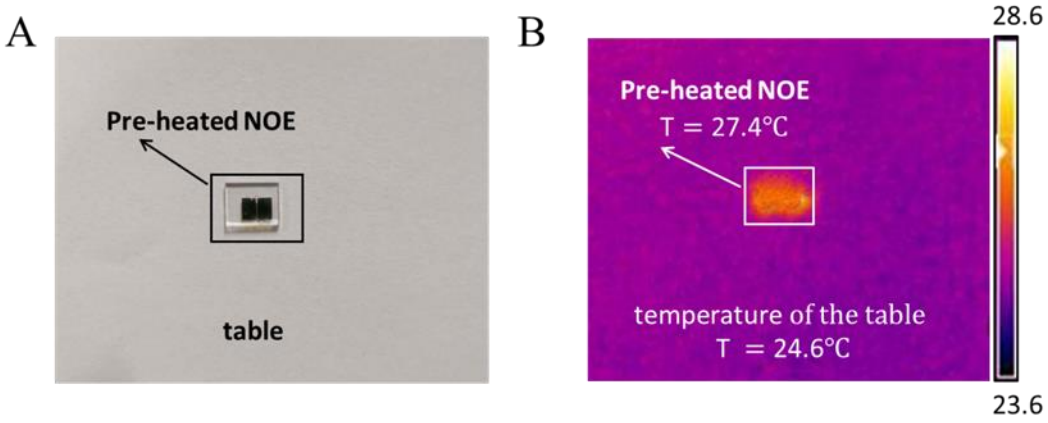

Figure S18. Optical and photothermal imaging of the NOE junction (A) Photograph of a pre-heated NOE device put on a table at room temperature. (B) Photothermal image of the pre-heated NOE junction. Note: The NOE was briefly pre-heated by a heating disk and then put on the table for the photothermal imaging. Related to Figure 4.

Note S1. Simple estimates of the current of NOE based on electron tunneling:

We can, with a simple, WKB-based model (see ref.: Tomfohr and Sankey, 2002), estimate the current density j (current per unit area) from

$$j \approx 2G_0 e^{-\beta L} V/a^2 \approx 2 \times 10^{-16} A/Å^2$$

where G_0 the quantum of conductance, 77 uS; β is a length decay factor (in nm^{-1}) and is a function of the energy (13.3 nm^{-1} for SiO_2 at 4 eV) and L is the thickness of the silica shell (1.8 nm). V is the applied bias (we will use 1 V, the maximum bias reached in our experiments) and a=5.06 Å, the lattice constant for the conventional unit cell used in SiO_2 band structure calculations.

To simplify the calculation, we assume that only a row of Au@SiO_2 NPs (~ 1.4×10^5, the same as the number of NOE measured in our experiments) bridges the Au electrode (see Scheme S1). The contact area is ~22,000 $Å^2$ (~area of hemisphere, in fact, the contact area between SiO_2 shell and Au electrode is much smaller(Salomon et al., 2003)). The tunneling probability is $e^{-\beta L}(\sim 4 \times 10^{-11})$ for a single 1.8 nm silica gap. Furthermore, electrons cross the electrode/NOE interface twice (from one electrode to the AuNP and then from AuNP to another electrode) to get from one electrode to the other one. Thus, the estimated current for the one row of Au@SiO_2 NPs-based NOE is ~3×10^{-17} A, which is 6 orders of magnitude less than the detected junction current (~10^{-11} A) for the whole NOE that bridges the 100 μm gap between the electrodes. Thus it is clear that transport cannot be by coherent tunneling between Au NPs, also as we would need ~ 6500 sequential tunneling events to cross the gap between the electrodes! Related to Figure 3.

Scheme S1. Simplified calculation model for the estimation of the transport current. Related to Figure 3.

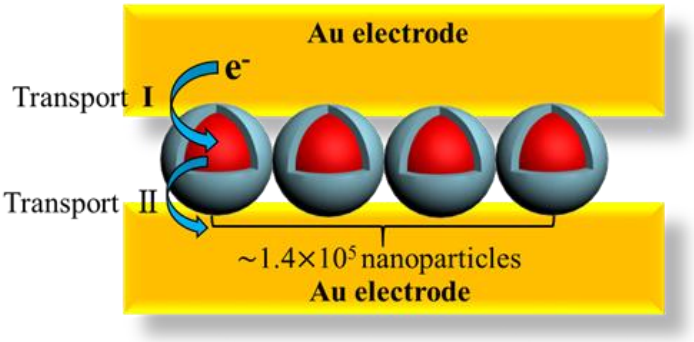

Note S2. In our junction system, the capacitance of the Au@SiO_2 NPs is about 4×10^{-18} F, as calculated by the following equation: (Abeles et al., 1975)

$$C = 4\pi\varepsilon_0\varepsilon_r\left(\frac{1}{R}-\frac{1}{R+s}\right)^{-1} = 4\pi\varepsilon_0\varepsilon_r\frac{R(R+s)}{s}$$

where ε_0 is the dielectric constant of vacuum [8.854×10^{-12} F/m], ε_r the relative dielectric constant of silica (ε_r =2.4),(Caillard et al., 2013) R is the radius of AuNPs [m], and s is the distance between AuNPs [m]. The estimated value, based on particle size, is in rough agreement with the experimental RT value ($C\approx e/\Delta V=1.3\times10^{-18}$ F, see Figure 3b).

Considering the electrostatic interaction between the nanoparticles, the corresponding charging energy, E [J] can be calculated by the following equation: (Abeles et al., 1975)

$$E = \frac{2e^2}{R}\left[\frac{\frac{s}{R}}{\varepsilon_0\varepsilon_r\left({}^{1}/_{2}+{}^{2s}/_{R}\right)}\right] \approx 1.4\times10^{-19}J$$

where e is the electron charge [1.6×10^{-19} C]. We see that this charging energy is much larger than the thermal energy k_BT (4×10^{-21} J) at RT. Meanwhile, according to the experimental result presented in Figure 3a, the resistance of the junction $R=V/I\approx 1V/10pA\approx10^{11}\,\Omega$, which is much larger than the quantum of resistance ($\hbar/e^2=2.6\times10^4\,\Omega$). Related to Figure 3.

Note S3. Temperature increase (ΔT) estimation:

According to an earlier report (Qin et al., 2012), the plasmon-induced temperature increase (ΔT) can be calculated as follows:

$$Q_{nano} = C_{abs}\times I$$

$$\Delta T_{nano} = {}^{Q_{nano}}/_{(4\pi k_s r_{NP})}$$

where Q_{nano} is the heat produced by the Au@SiO_2 NPs [W], C_{abs} is the optical absorption cross-section area of AuNPs [m^2], I is the light intensity impinging on the nanomembranes [W/m^2], r_{NP} is the particle radius [m], and k_s is the thermal conductivity of the silica [$W\cdot m^{-1}\cdot K^{-1}$].

In our system, I = 0.086 W/cm^2, $r_{NP}=6\times10^{-9}$ m, k_s = 0.52 $W\cdot m^{-1}\cdot K^{-1}$ (for silica

shell), and C_{abs} = ~3×10^{-15} m^2. Then, the temperature increase ΔT_{nano} is calculated to be ~ 6.5×10^{-5} K ＜ 1 K. Thus, the photothermal effect should not be the main driving force for the electron transfer enhancement. Related to Figure 4.

Transparent Methods

Materials and chemicals

Sodium citrate, sodium silicate, polyvinyipyrrolidone (PVP, Mw~55000), (3-Mercaptopropyl)trimethoxysilane (MPTMS) and ethylene glycol (EG) were purchased from Sigma-Aldrich. 3-aminopropyltrimethoxysilane (APTMS) were purchased from Alfa Aesar. $HAuCl_4\cdot4H_2O$ were purchased from Beijing Chemical Factory (Beijing, China). Na_2PdCl_4 were purchased from Aladdin reagent company (Shanghai, China). All of the chemicals were used without further purification. Water used throughout all these experiments was purified with a Millipore system (18.2 M Ω • cm) .

Synthesis of free-standing monolayered nanomembranes of $Au@SiO_2$ NPs and $Pd@SiO_2$ NPs.

The colloidal Au nanoparticles used in our experiments were synthesized using a method described previously.(Frens, 1973; Haiss et al., 2007) $Au@SiO_2$ nanoparticles with different silica shell thickness were synthesized by the method reported by Tian's group and our previous work.(Li et al., 2017; Li et al., 2010) The free-standing monolayered nanomembranes were prepared by the method of liquid/liquid interface self-assembly. Typically, 3 mL $Au@SiO_2$ core-shell NPs were poured into a plastic container, and about 460 uL hexane were added to the solution to form liquid/liquid interface, then 3.7 mL methanol was poured into the mixture rapidly to capture the nanoparticles at the hexane/water interface. After the evaporation of hexane, the nanoparticles were simultaneously self-assembled into monolayer over a large area at the water/hexane interface.

The 12 nm Pd NPs were prepared according to the method reported by Xia's group.(Xiong et al., 2005) The product was added to 33 mL of acetone, followed by centrifugation at 4000 rpm for 5 min. Then the precipitate was collected and redispersed in 10 mL of ethanol. A volume of 40 mL of hexane was added to the dispersion, and the solution was centrifuged at 4000 rpm for 5 min. The precipitate was washed twice and finally, the precipitate was dispersed in 200 mL of water.

$Pd@SiO_2$ NPs were synthesized by the same method described above except using MPTMS as coupling reagent instead of APTMS.

Fabrication of the NOE junctions.

Gold trench electrodes (~20 nm thick) with a 100-μm gap were prepared by thermally evaporating Au on the glass substrate, using a shadow mask technique in vacuum at 10^{-4} Pa. The NOE junction structures were fabricated by transfer of the monolayererd $Au@SiO_2$ NP nanomembranes gently from the "soft" air-water interface onto the Au trench electrodes. The devices were thoroughly air-dried before the electrical measurements.

Characterizations.

The morphologies of the $Au@SiO_2$ NPs and Au NPs were characterized with a JEOL-2100F transmission electron microscope (TEM) and spherical aberration-corrected scanning transmission electron microscope (Cs-corrected STEM, Titan G2 60-300). The morphologies of the junctions were characterized with a XL30 ESEM scanning electron microscope (SEM). Atomic force microscopy (AFM) was done with a Multimode 8 atomic force microscope (Bruker, Germany) in the tapping mode. The UV−Vis absorption spectra were obtained using a UV-2600 spectrophotometer (Shimadzu, Japan). Microscopy-based selected area bright-field extinction spectra and dark-field scattering images were obtained using an inverted Leica DMI6000B microscope (Germany) connected with a USB 4000 spectrometer (Ocean Optics, Inc.). Room-temperature current-voltage (I-V) characteristics of the junctions were recorded at ambient conditions using a Keithley 2636B source meter, and lasers with different wavelengths (with equal light intensity of 35 mW) were used for illumination. Photothermal imaging of the junctions was done with a thermal infrared imager (Fluck, TiS 40).

SUPPLEMENTAL REFERENCES

Xiong, Y., Chen, J., Wiley, B., Xia, Y., Aloni, S., and Yin, Y. (2005). Understanding the Role of Oxidative Etching in the Polyol Synthesis of Pd Nanoparticles with Uniform Shape and Size. J. Am. Chem. Soc. *127*, 7332-7333.